

---

---

ACOUSTIC SIGNALS PROCESSING.  
COMPUTER SIMULATION

---

---

## Approach to Detecting Aberrations in Transcranial Ultrasound Imaging

D. V. Leonov<sup>a, b, \*</sup>, N. S. Kulberg<sup>a, c, \*\*</sup>, T. V. Yakovleva<sup>c, \*\*\*</sup>, and P. D. Solovyova<sup>b</sup>

<sup>a</sup> Scientific and Practical Clinical Center for Diagnostics and Telemedicine Technologies, Moscow Department of Health, Moscow, 127051 Russia

<sup>b</sup> National Research University MPEI, Moscow, 111250 Russia

<sup>c</sup> Federal Research Center “Computer Science and Control” of Russian Academy of Sciences, Moscow, 119333 Russia

\*e-mail: LeonovD.V@ya.ru

\*\*e-mail: kulberg@ya.ru

\*\*\*e-mail: tan-ya@bk.ru

Received August 23, 2021; revised November 27, 2021; accepted November 30, 2021

**Abstract**—The presence of cranial bones in the ultrasound propagation path seriously complicates the imaging of tissues and blood vessels of the brain since the bones distort the ultrasound field, introducing phase and amplitude aberrations. Such distortions are not always apparent since complete information about the studied object is fundamentally inaccessible. The article develops a new approach that uses the synthetic aperture method to detect wavefront aberrations. A quantitative parameter is proposed that characterizes the presence of aberrations by measuring the RMS width of the angular intensity distribution. Experimental results were obtained at a frequency of 2 MHz using phantom and *in vivo* transcranial data. It is shown that in the presence of aberrations, the value of the proposed parameter increases by 22–45% with respect to the theoretical value for the aberrationless case.

**Keywords:** focused ultrasound, phase correction, phantom, synthetic aperture, beamforming, focusing, diagnostic imaging

**DOI:** 10.1134/S106377102202004X

### INTRODUCTION

Transcranial ultrasound is used for diagnosing pathological changes in tissues and blood vessels of the brain and noninvasive surgical intervention. In diagnostics, small phased sensors and thin acoustic windows in the skull are used; in surgery, large and powerful hemispherical emitters are used, capable of creating a field that passes even through thick bones [1–7]. However, wave refraction in the skull and at soft-tissue boundaries reduces the focusing quality, leading to a deterioration in contrast and spatial resolution and, as a result, loss of diagnostic information [1]. This is due to sound speed and density differences between bone and soft tissues [2]. The temporal transparency window is often used in transcranial diagnostics since it is the thinnest ( $2.7 \pm 0.9$  mm corresponds to good acoustic permeability [3]) and features a wide field of view. Its difference from soft tissues in terms of sound speed (2570–3030 m/s), as well as its high attenuation (from 379 to 1210 Np/m) and uneven surface, contributes to the occurrence of aberrations [4].

There are several approaches to assessing the focusing quality of ultrasound radiation in transcranial studies [7–14]. One of the first attempts at such an

assessment was proposed by M. Fink [15]. In this case, it was necessary to introduce a hydrophone into the region of interest. The signal from the hydrophone was received by a phased sensor applied to the skull. The received front was compared with a spherical one, delays and attenuation were calculated, and a conclusion was drawn about the focusing quality. Due to its invasiveness, this procedure has not been widely implemented in clinical practice, but it has become the gold standard in scientific research and has been repeatedly modified [16–18].

Thanks to improved design techniques and excitation methods, multi-element phased arrays are widely applied in surgery [5–7]. However, the ultrasound arrays used in surgery work only in transmission mode, so computer simulation of acoustic field propagation from a target through the brain tissue and skull bones to an ultrasound transducer has become promising for aberration correction techniques [19–22]. This approach preliminarily assesses the acoustic properties of the skull obtained from the computer or magnetic resonance tomograms. The approach applies three main numerical simulation strategies: the ray tracing [23], the angular spectrum

method [24], and the simulation that takes into account the pulse shape [25, 26]. The last strategy yields the most accurate estimate [27], but the simulation takes several hours, making it inappropriate for clinical use. There is also a method called MR acoustic radiation force imaging (MR-ARFI) [28], where MRI motion-sensitive encoding gradients, similar to those used in MR elastography, are implemented to measure the micron-scale static tissue displacement induced by ultrasound waves as phase shifts in the resulting MR image [7]. Since this tissue displacement is proportional to the local acoustic intensity, MR-ARFI allows noninvasive pressure measurements and their usage for selecting appropriate phase delays to compensate for the contribution of the aberrating layer.

The article proposes a new approach to detecting wavefront distortions in transcranial ultrasound imaging based on the synthetic aperture method [29]. The distortion detection method estimates the beamwidth; there is no distortion if the beam is sufficiently narrow. The term “beam” refers to the area in which the most significant radiation energy is concentrated; it is characterized by the beamwidth that varies with distance from the emitter and takes the smallest value at the focus. The widening occurs due to defocusing caused by the passage of the beam through the aberrating layer, which introduces additional delays not taken into account during beamforming, which consists in the coherent summation of signals from all elements of the phased array. A significant advantage of the proposed approach is that it requires only one phased sensor; the region of interest does not necessarily contain point sources.

## MATERIALS AND METHODS

### *Aberration Detection Method*

A new approach to detecting aberrations involves applying the ultrasound probe to the object’s surface, filling the intermediate space with ultrasound gel or other sound-conducting substance. Then, the ultrasound transducer emits and receives signals in the synthetic aperture mode, which are preprocessed in the path of the ultrasound device.

Conventional synthetic aperture scanning consists of the following steps:

- selection of a direction angle and formation of the transmitter beam in that direction;
- formation of the receiver beam in a direction coinciding with that of the transmitter beam;
- storage of the received signal value in memory;
- repetition of the previous steps for each angle in the range corresponding to the region of interest.

An essential distinguishing feature of the proposed approach is the use of a special diagnostic scanning scheme with the following steps:

- selection of the angle for which the correction will be carried out;
- fixation of the angle for transmit beamforming;
- scanning each angle in the region of interest during receive beamforming;
- storage of the received signals.

If there are no aberrations, such a scanning scheme yields an image where the brightest area corresponds to the selected correction angle. The presence of aberrations will expand the bright region since aberrations broaden both the transmitter and receiver beam. Figure 1 visually explains this principle. There is no distorting plate in the left image, so the angular beamwidth  $\Delta$  is smaller than in the right image.

Thus, in the proposed method for detecting aberrations, the response function of a set of virtual point sources is constructed, located one after another so that each has a unique radial coordinate. Still, the angular coordinate is the same for all. Virtual point sources are formed by the synthetic aperture method: the first element of the array emits first, and all of them receive, then the second element emits, and all receive, etc., the process repeats for each element. Aperture synthesis is characterized by focusing on reception and transmission at the postprocessing stage. The presence of aberrations broadens the response function, and this broadening of the angular coordinate can be expressed as a quantitative parameter.

### *Equipment for Experimental Testing*

The main element of the experimental setup was a Sonomed-500 device manufactured by Spectromed (Moscow) with a 3.0S19 sectoral phased sensor from Medelcom (Vilnius, Lithuania) containing 64 piezoceramic elements with a step of 290  $\mu\text{m}$ , a transverse dimension of 13 mm, and a band of 1.6–3.7 MHz for a level of  $-3$  dB. For further processing on a computer, the ultrasound diagnostic device can transmit raw signals from the B-imaging path taken in the synthetic aperture mode. The signals underwent some preliminary processing in the device path (amplification, bandpass filtering, Hilbert transform). The signals are captured and stored in the memory before they reach the input of the beamformer. In all the experiments ultrasound probe emitted the signals at a carrier frequency of 2 MHz.

The observations were made with an ATS Laboratories Model 539 multipurpose phantom [30]. Its overall dimensions were  $23.4 \times 20.5 \times 9.5$  cm, the sound speed in the phantom was 1450 m/s, and the ultrasound attenuation coefficient was  $0.5 \text{ dB cm}^{-1} \text{ MHz}^{-1}$ . The phantom is made of urethane rubber and includes nylon strings 120  $\mu\text{m}$  in diameter, designed for testing the spatial resolution, and grayscale targets of various sizes and echogenicity. The phantom is engineered to monitor the following characteristics: penetration depth, evaluation of the spatial and contrast resolu-

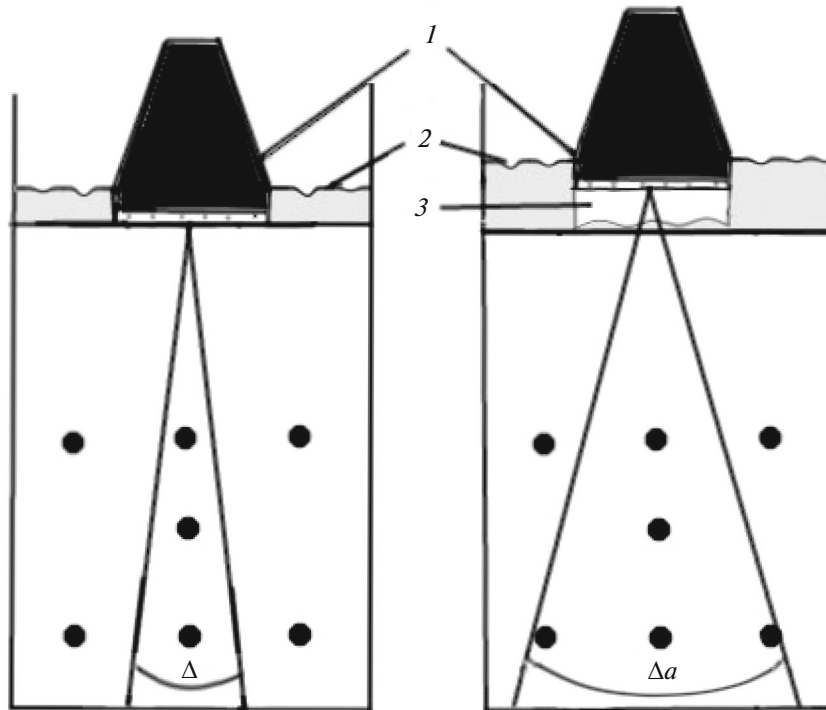


**Fig. 1.** Explanation of aberration detection method. (1) Sector ultrasound sensor; (2) sound-conducting material; (3) distorting layer;  $\Delta$ , angular beamwidth.

tions. The targets in the phantom are distributed according to the scheme in Fig. 2.

In most experiments, the sensor was mounted on a stand to minimize the effect of random vibrations. Aberrations were introduced using specially made distorting plates. The plates were cast of EKON waterproof silicone gel (Moscow), in which the sound propagation velocity after solidification is 1200 m/s. In the process of plates preparation, the molds were 3D printed from PLA plastic and filled with liquid gel. The aberrators are plates  $35 \times 26$  mm in size and 3 to 5 mm thick. The shape of the aberrator is given by the harmonic function  $A \sin(2\pi n l / L)$ , where  $A = 1$  mm is the amplitude of the surface deviation,  $L = 20$  mm is the aperture width of the phased sensor, and  $n$  is the number of sinusoid periods that fit on the sensor surface. Two aberrators were prepared in such a way: No. 1 ( $n = 1.5$ ) and No. 2 ( $n = 2.5$ ). A fastener was made on a 3D printer from PLA plastic and attached the plates to the sensor surface.

Aberrator No. 3 was ex vivo temporal bone; prior to the study it was placed in a pressure chamber for degassing. Just like other aberrators, the temporal bone was applied to an ATS Laboratories Model 539 phantom, and the space between the temporal bone, phantom and transducer was filled with ultrasound gel.

One of the experiments was conducted in vivo. In this case, a phased ultrasound transducer was applied through a sound-conducting gel to a volunteer's head

in the area of the temporal acoustic window. In all of the experiments, the scanning was performed in the synthetic aperture mode.

The device and method described in [16] were used to obtain the profiles of phase distortions introduced by each of the aberrating layers. In this case, the signal from a single-element pencil-type sensor located on the axis passing through the center of the sonogram on the opposite side of the phantom or head and acting as a calibration source passed through the object under the study and arrived at the aperture of the phased sensor. In the absence of an aberrator at the aperture of the phased sensor, a spherical wavefront emitted by a single-element sensor is recorded, and the radius of the spherical front corresponds to the distance between the sensors. Distorting layers introduce delays into the phase front, which are detected from the deviation from sphericity; these delays yielded the profiles shown in Fig. 3.

#### *Course of the Experiment*

The sector phased ultrasound transducer is applied to the phantom so that objects enter the field of view to test the spatial resolution, as shown in Fig. 1. The space between the radiating surface of the sensor and the phantom is filled with degassed water. The ultrasound transducer scans in the synthetic aperture mode and forms a data file in the device memory, which can be transferred to a computer for further processing and

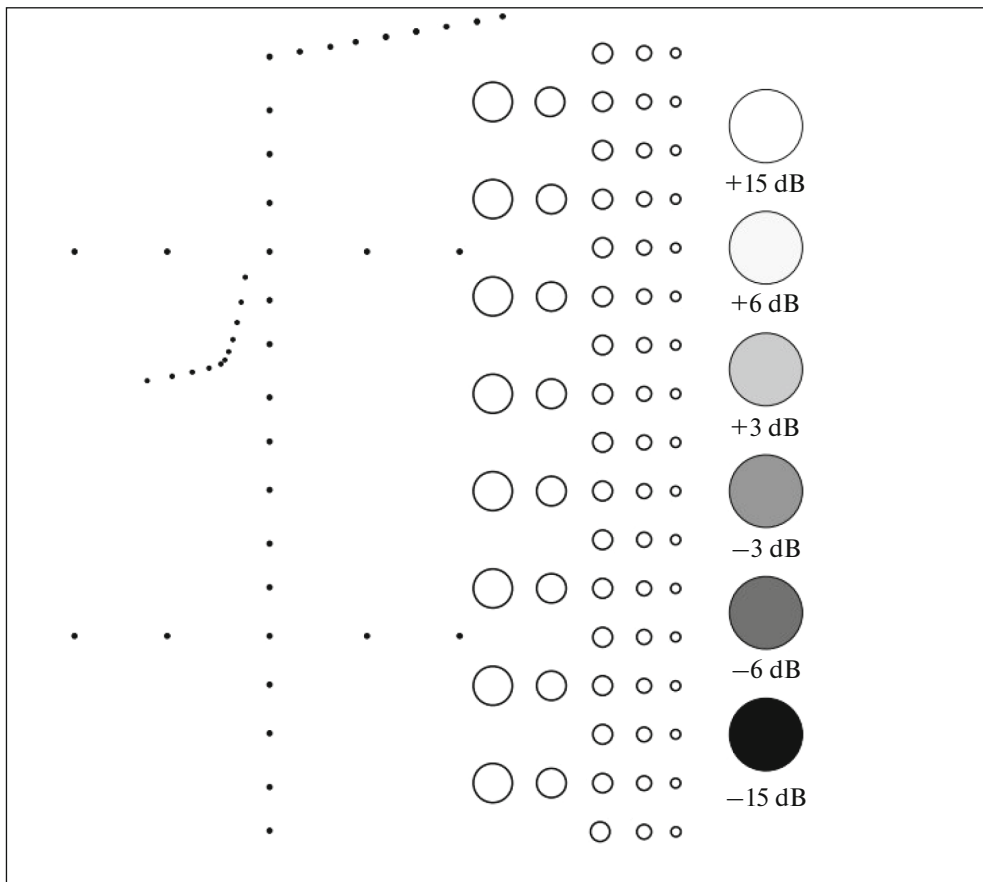


Fig. 2. Diagram of location of objects in ATS Laboratories Model 539 phantom.

sonogram imaging. During the scanning process, the signal is emitted by the first element of the sensor, propagates in the phantom, is reflected, and received by all sensor elements, each of which records the received signal in its own channel. After that, emission and reception are repeated for each of the sensor elements. As a result, a data file  $P$  of size  $K \times K \times N$  is formed, where  $K$  is the number of sensor elements and  $N$  is the number of depth samplings.

Then, the aberrating layer is placed in the space between the sensor surface and the phantom. The scanning procedure described in the previous paragraph is repeated for each of the aberrating plates. As a result, we obtain  $B + 1$  data files  $P$ , where  $B$  is the number of distorting plates. Thus, a data file without an aberrator and three data files with different aberrators were obtained. A fifth set was obtained by ultrasound examination of the head of a volunteer; the other files used the distorting layers described in the subsection Equipment for Experimental Testing. The acquired data is transferred to a computer for further processing.

On the computer, a code is run in Microsoft Visual Studio that reads the data and constructs a sonogram

for each of the data files  $P$ . To construct a sonogram, the conventional and proposed scanning schemes with synthetic aperture described in the subsection Aberration Detection Method were used.  $2B + 2$  sonograms are generated, for each of which the following parameters are estimated:

(a) the RMS width of the angular intensity distribution:

$$\alpha = \frac{\sqrt{\int_a^b A(\varphi)(\varphi - \varphi_0)^2 d\varphi}}{\sqrt{\int_a^b A(\varphi) d\varphi}}, \tag{1}$$

where  $\varphi$  is the angle that determines the inclination of the probing beam;  $A(\varphi)$  is the angular intensity distribution;  $\varphi_0$  is the position of the intensity peak; since focusing on transmission is performed for a zero angle,  $\varphi_0 = 0^\circ$ ;  $a$  and  $b$  are the integration limits determined by the decrease in intensity; in our case, integration was performed from  $-15^\circ$  to  $15^\circ$ ;

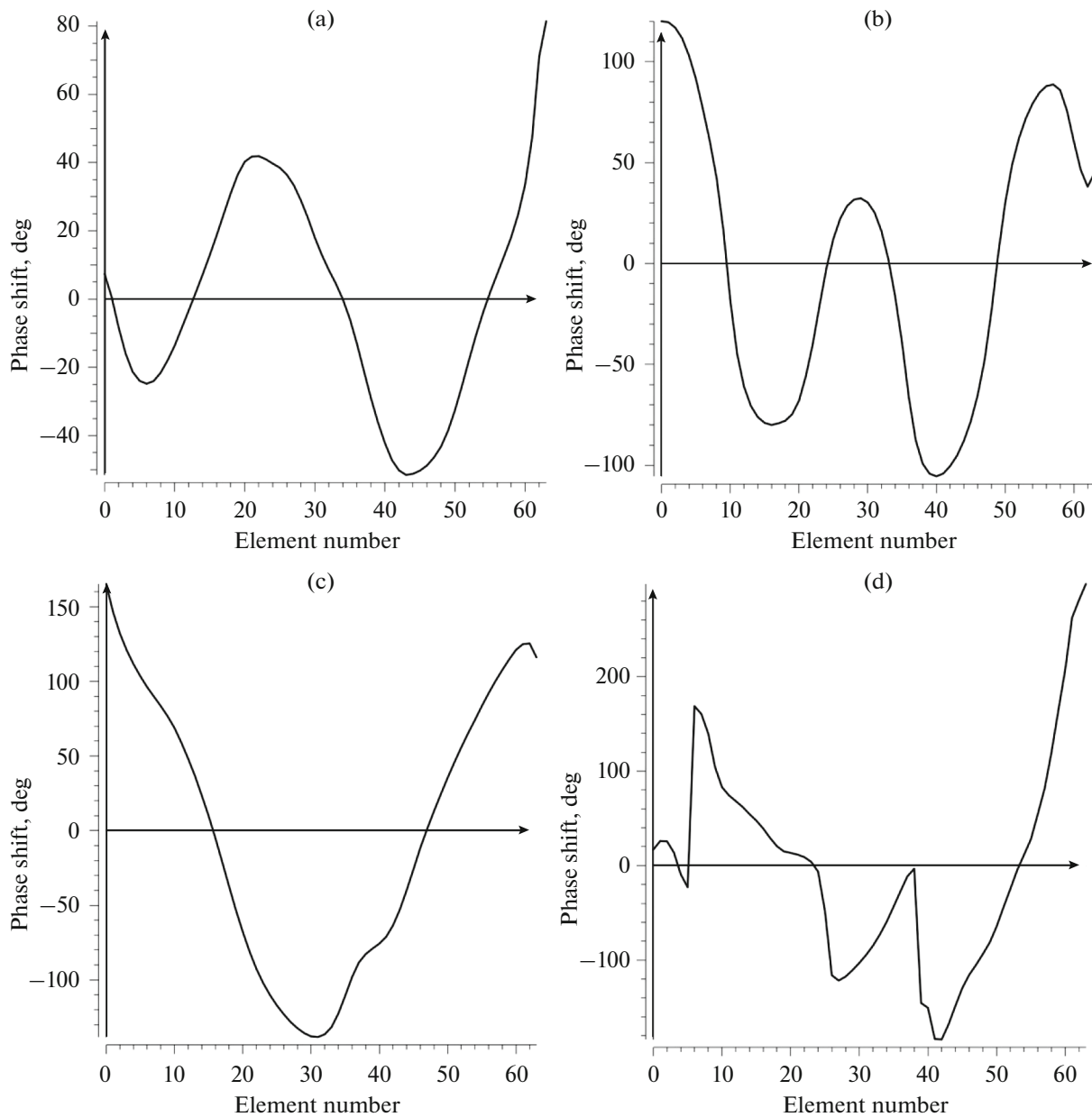


**Fig. 3.** Phase distortion profiles introduced from aberrators: (a) aberrator No. 1, (b) aberrator No. 2, (c) aberrator No. 3, (d) skull bone during in vivo brain ultrasound. Horizontal axis, number of phased array element; vertical axis, phase shift, deg.

(b) integrated intensity normalized to the peak value:

$$\beta = \frac{\int_{-45^\circ}^{45^\circ} A(\varphi) d\varphi}{A_{\max}}, \quad (2)$$

where  $A_{\max}$  is the intensity value at the distribution peak;

(c) the central value of the intensity angular distribution function:

$$\gamma = A(0^\circ); \quad (3)$$

(d) the width of the main lobe of the angular intensity distribution of the echo signal at a level of 0.707 of the intensity value at the center of the distribution:

$$\begin{cases} \delta = \varphi_R - \varphi_L, \\ \varphi_R = \varphi, \text{ if } A(\varphi) = 0.707A_{\max} \wedge \varphi < 0^\circ, \\ \varphi_L = \varphi, \text{ if } A(\varphi) = 0.707A_{\max} \wedge \varphi > 0^\circ, \end{cases} \quad (4)$$

where  $\varphi_L$  and  $\varphi_R$  are the left and right boundaries of the main lobe;

(e) mode  $\varepsilon$  as the most frequently encountered value in the data set:

$$\varepsilon = \max(\text{hist}(\text{LPF}(A(\varphi)))) \quad (5)$$

where  $\max$  is the function of finding the distribution value at the peak,  $\text{hist}$  is the histogram construction operator, and  $\text{LPF}$  is low-pass filtering;

(f) the RMS width of the angular intensity distribution after mode subtraction:

$$\zeta = \sqrt{\frac{\int_a^b (A(\varphi) - \varepsilon)(\varphi - \varphi_0)^2 d\varphi}{\int_a^b (A(\varphi) - \varepsilon) d\varphi}} \quad (6)$$

The parameters are estimated from the angular intensity distribution obtained at a distance of 100 mm from the aperture of the ultrasound sensor.

## RESULTS

The results of the study are presented in Tables 1–3. It can be seen that when the proposed scanning scheme is used, the value of parameters  $\alpha$ ,  $\beta$ ,  $\delta$ ,  $\varepsilon$  and  $\zeta$  is greater when there are aberrations, while the value of  $\gamma$ , conversely, decreases. Thus, the presence of aberrations increases the RMS width of the angular intensity distribution  $\alpha$  by 31% if we compare the cases of absence of an aberrator and ultrasound through skull bones. When the conventional scanning scheme was used, it was not always possible to determine the distribution width  $\delta$ ; parameter  $\alpha$  hardly changed at all when an aberrator was added,  $\gamma$  decreased, and the other parameters increased.

## DISCUSSION

Phase aberrations occur when there is a medium on the wave propagation path in which the sound propagation velocity differs from the main medium and the boundary of the media is not smooth. Energy losses occur when the acoustic impedance of one medium differs from the impedance of the other. Both these phenomena were observed in the aberrators.

Since aberrators No. 1 and No. 2 are made of the same material, the attenuation coefficient of the ultrasound wave in them is the same, but the profile of introduced phase distortions differs. As seen from Fig. 3, aberrator No. 2 introduces a larger phase shift than aberrator No. 1. Quantitatively, this is confirmed by parameters  $\alpha$ ,  $\beta$ , and  $\delta$  when the proposed scanning scheme is used. Parameter  $\gamma$ , conversely, increased, although the expansion of the lobe should have led to its decrease. Such a result may be due to the slight shift in the position of the sensor caused by the aberrator replacement and the influence of the nylon wires to check the resolution in the phantom.

The value of the distribution width  $\delta$  calculated from the threshold level of 0.707, as can be seen from Table 3, is a possible additional criterion for the pres-

ence of aberrations when the proposed scanning scheme is used. The presence of aberrators leads to an increase in this parameter by 16.3–295.3%. Parameter  $\delta$  is very sensitive to the choice of threshold level and is not applicable to the conventional scanning scheme due to the impossibility of taking into account a significant part of the angular spectrum outside the threshold level specified for calculating parameter  $\delta$ .

The calculated parameters can be affected not only by phase distortions, but also by energy losses that invariably occur at the boundaries of the media and in the media themselves. If we multiply  $\beta$  and  $\gamma$ , then we obtain the estimate for energy losses. Thus, the addition of aberrator No. 1 resulted in a loss in intensity of 46% versus case without an aberrator. When aberrator No. 3 was used, 87% of the signal intensity was lost.

It follows from the above that parameter  $\alpha$  with combination with the proposed scanning scheme can be an effective quantitative criterion in determining the presence of aberrations, since it changes steadily by 20–31% when aberrations occur, while in the conventional scheme, it is not informative.

The only requirement for the implementation of the proposed method is the availability of at least two datasets obtained using the proposed scanning scheme and the same settings of the ultrasound device. Moreover, one of the sets must certainly contain the reference data obtained in the study of the object without aberrations. The second and subsequent sets may contain aberrations. It is their comparison with the reference set in the described way that allows us to speak about the presence or absence of aberrations. However, this requirement is not mandatory, since it is possible to compare with the theoretical value.

The spatial distribution of the acoustic pressure is described by the Helmholtz equation [31]:

$$(\Delta + k^2)p(t, x) = f(t, x), \quad (7)$$

where  $\Delta = \nabla^2$  is the Laplace operator;  $k = \frac{\omega}{c}$  is the wave vector modulus;  $f(t, x)$  is the source response;  $t$  is time;  $p(t, x)$  is the sought pressure distribution, which, after it is recorded by the ultrasound phased array, can be represented in the frequency domain as the following function:

$$p(\omega, x) = \int_{-b/2}^{b/2} a(x')G(\omega, x - x')dx', \quad (8)$$

$$G(\omega, r) = \frac{\exp\left(i\frac{\omega}{c}r\right)}{r} = \frac{\exp\left(i\frac{\omega}{c}\sqrt{(x - x')^2 + z^2}\right)}{\sqrt{(x - x')^2 + z^2}}, \quad (9)$$

where  $G(\omega, x)$  is the Green's function of the Helmholtz equation [32];  $a(x)$  is the aperture function, including apodization, as well as the phase shift ensuring focusing to depth  $z$ ;  $i$  is the imaginary unit;  $\omega$  is the

**Table 1.** Comparison of conventional and proposed scanning schemes

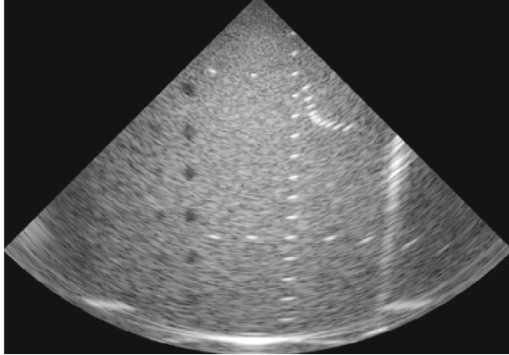
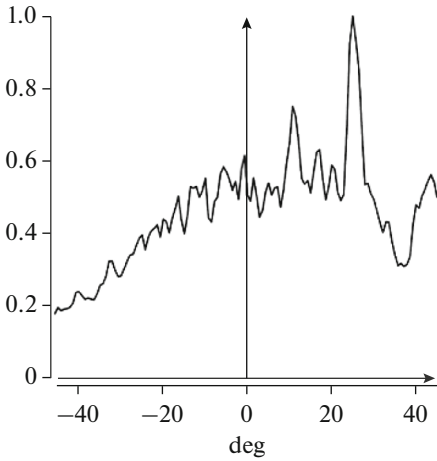
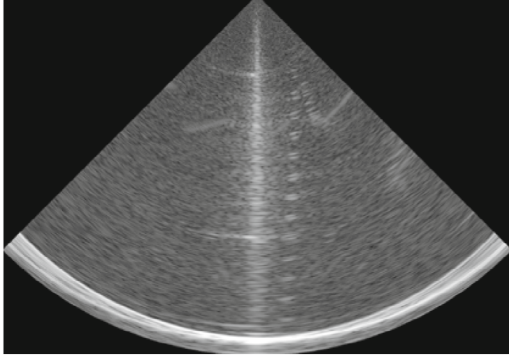
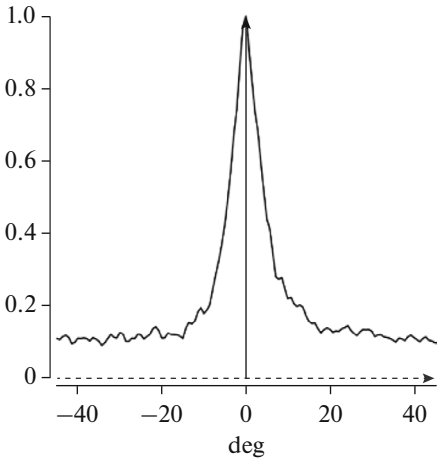
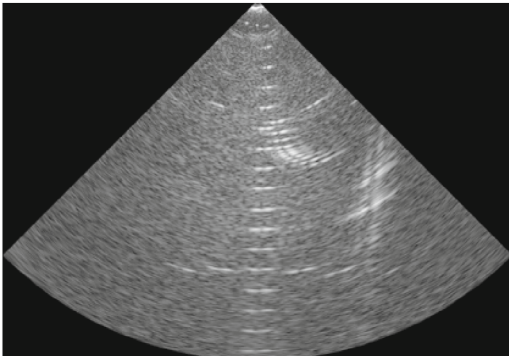
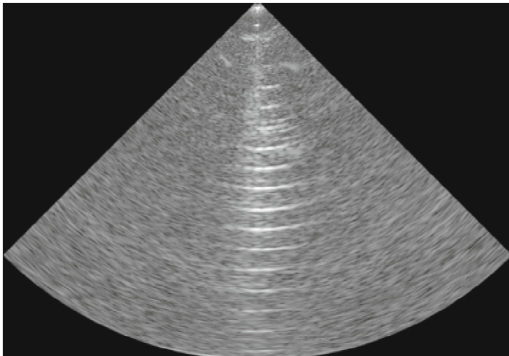
	Conventional scanning scheme	Proposed Scanning Scheme
	sonogram/angular intensity distribution of echo signals	sonogram/angular intensity distribution of echo signals
No aberrations	 	 
Aberrator No. 1		

Table 1. (Contd.)

	Conventional scanning scheme	Proposed Scanning Scheme
	<p>A line graph showing a broad, multi-peaked distribution of values. The x-axis is labeled 'deg' and ranges from -40 to 40. The y-axis ranges from 0 to 1.0. The curve starts at approximately 0.25 at -40 degrees, rises to a peak of about 1.0 at 0 degrees, and then exhibits several smaller peaks and troughs as it descends towards 40 degrees.</p>	<p>A line graph showing a sharp, narrow peak centered at 0 degrees. The x-axis is labeled 'deg' and ranges from -40 to 40. The y-axis ranges from 0 to 1.0. The curve is relatively flat at approximately 0.25 for most of the range, with a very sharp peak reaching 1.0 at 0 degrees.</p>
Aberrator No. 2	<p>A sector-shaped image showing significant horizontal streaking artifacts, indicating poor resolution or focus in the conventional scanning scheme.</p> <p>A line graph showing a broad, multi-peaked distribution of values. The x-axis is labeled 'deg' and ranges from -40 to 40. The y-axis ranges from 0 to 1.0. The curve starts at approximately 0.25 at -40 degrees, rises to a peak of about 1.0 at 0 degrees, and then exhibits several smaller peaks and troughs as it descends towards 40 degrees.</p>	<p>A sector-shaped image showing a much smoother and more uniform appearance, indicating improved resolution or focus in the proposed scanning scheme.</p> <p>A line graph showing a sharp peak at 0 degrees. The x-axis is labeled 'deg' and ranges from -40 to 40. The y-axis ranges from 0 to 1.0. The curve is relatively flat at approximately 0.25 for most of the range, with a sharp peak reaching 1.0 at 0 degrees.</p>
Aberrator No. 3	<p>A sector-shaped image showing horizontal streaking artifacts, similar to the conventional scheme.</p>	<p>A sector-shaped image showing a smoother appearance, similar to the proposed scheme.</p>

Table 1. (Contd.)

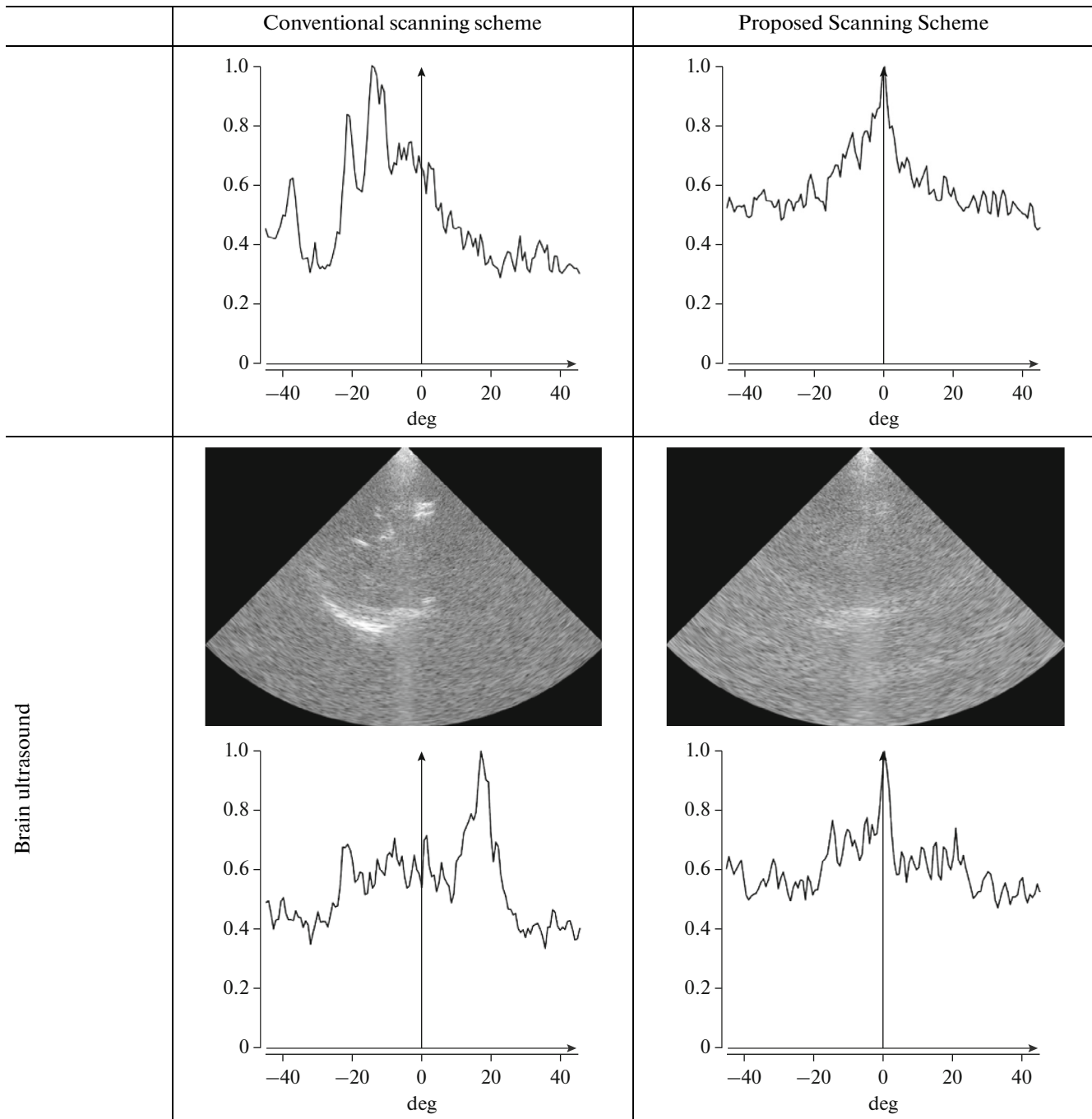


Table 2. Criteria for presence of aberrations when using proposed scanning scheme

	RMS width of angular intensity distribution ( $\alpha$ ), deg	Normalized integral intensity ( $\beta$ ), arb. units	Value of function at center ( $\gamma$ ), arb. units	Distribution width at threshold level 0.707 ( $\delta$ ), deg	Mode value ( $\epsilon$ )	RMS width of angular intensity distribution after mode subtraction ( $\zeta$ ), deg
No aberrations	6.2	27	147	4.3	0.101	5.29
Aberrator No. 1	7.5	47	45	5.0	0.260	6.34
Aberrator No. 2	7.9	63	54	17.0	0.293	7.54
Aberrator No. 3	8.0	77	7	9.2	0.511	7.12
Brain ultrasound	8.2	79	4	5.7	0.506	7.52

**Table 3.** Criteria for presence of aberrations for conventional scanning scheme (“–”, parameter undetermined)

	RMS width of angular intensity distribution ( $\alpha$ ), deg	Normalized integral intensity ( $\beta$ ). arb. units	Value of function at center ( $\gamma$ ), arb. units	Distribution width at threshold level 0.707 ( $\delta$ ), deg	Mode value ( $\epsilon$ )	RMS width of angular intensity distribution after mode subtraction ( $\zeta$ ), deg
No aberrations	8.5	59	170	–	0.046	4.81
Aberrator No. 1	8.5	61	50	14.9	0.249	8.39
Aberrator No. 2	8.2	73	74	12.8	0.253	7.98
Aberrator No. 3	8.4	63	13	–	0.306	8.74
Brain ultrasound	8.6	70	17	0.7	0.378	8.72

ultrasound oscillation frequency;  $c$  is the sound speed in the medium;  $z$  is the distance from the scatterer under the study to the aperture of the phased sensor;  $x$  is the coordinate along the surface of the aperture.

Equation (8) in the Fresnel approximation can be represented as

$$p(\omega, x) = \int_{-\xi_0}^{\xi_0} \tilde{a}(\xi) \exp(-ix\xi) d\xi, \quad (10)$$

where the variable substitution is used  $\xi = -\frac{\omega x'}{zc}$ ,

$\tilde{a}(\xi) = a\left(-\frac{\xi zc}{\omega}\right) = a(x')$ . Equation (10) is the Fourier transform of the aperture function.

In our implementation of the method, rectangular apodization function was used:

$$a(x') = \begin{cases} 1, & \text{if } \frac{-D}{2} < x < \frac{D}{2}, \\ 0, & \text{otherwise,} \end{cases} \quad (11)$$

where  $D$  is the size of the ultrasound sensor aperture. As a result, we obtain

$$p(\omega, x) = \int_{-\xi_0}^{\xi_0} \exp(-ix\xi) d\xi = 2 \frac{\sin(x\xi_0)}{x}, \quad (12)$$

$$\xi_0 = \frac{\omega D}{2zc}, \quad (13)$$

$$p(\omega, x) = 2 \frac{\sin\left(\frac{x\omega D}{2zc}\right)}{x}. \quad (14)$$

Then, the value of the parameter  $\alpha$  is calculated with respect to  $x$ , which is called  $\alpha_{lin}$ :

$$\alpha_{lin} = \sqrt{\frac{\int_{x_l}^{x_r} p(\omega_0, x)(x - x_0)^2 dx}{\int_{x_l}^{x_r} p(\omega_0, x) dx}}, \quad (15)$$

where  $x_0$  is the coordinate of the distribution peak; the integration limits  $x_r$  and  $x_l$  are determined from the

previously selected range for calculation in the equation (1):

$$\begin{cases} x_r = z \tan(b), \\ x_l = z \tan(a). \end{cases} \quad (16)$$

Then, we calculate ion the RMS width (1) of the angular intensity distribution of the echo signal in terms of the calculated value :

$$\alpha = \arctan\left(\frac{\alpha_{lin}}{z}\right). \quad (17)$$

The value of  $\alpha$  is compared with that obtained from the experiment, and a conclusion is drawn about the presence of aberrations. For our parameters, the theoretical value of the RMS width of the angular intensity distribution obtained by numerical calculations with equation (17) is  $5.2^\circ$ . This value is 19% less than that obtained experimentally for a phantom without an aberrator. The theoretical value differs by 44–58% from the experimentally obtained values for aberrators and in vivo ultrasound of the brain.

The obtained difference between the experimental and theoretical values is quite significant. It may be associated with an inaccurate value of the aperture size, a possible shift in the carrier frequency, and the presence of speckle noise. Parameter  $\zeta$  was also calculated during the experiment, which differs from  $\alpha$  by the mode value. The mode value takes into account the contribution from speckle noise, so the comparison of the experimental  $\zeta$  and theoretical  $\alpha$  yields close results. Thus, the theoretical value of the RMS width of the angular intensity distribution  $\alpha$  obtained by numerical calculations with equation (17) is 1.7% smaller than the experimentally obtained  $\zeta$  value for a phantom without an aberrator. The theoretical value differs by 22–45% from the experimentally obtained values for aberrators and ultrasound of the brain.

It is incorrect to compare the theoretical value of the RMS width of the angular intensity distribution  $\alpha$  and experimentally obtained  $\zeta$  value for the conventional scheme, since for the conventional scanning scheme there may not be a point source at the center, like, e.g., in the presented case without aberration, which is why the empirical value of  $\zeta$  was less than the theoretical limit.

We believe that the proposed method for detecting aberrations can be particularly useful in the situation when the lack of a priori knowledge about the internal structure of the object under the study prevents a conclusion on the presence of aberrations based only on visual analysis of a sonogram using the conventional scanning scheme. It can also be helpful in developing aberration correction methods. For example, our team has developed an iterative method for correcting aberrations that approximates the phase distortions using low-order polynomials [29], in which the proposed approach to detecting aberrations makes it possible to quantify the quality of the correction and thus calculate at what iteration the correction algorithm should complete its work. The proposed method will be useful if the apodization function is chosen to decrease the side lobes.

One direction for the proposed method can be its extension to the entire frame by evaluating aberrations in multiple areas and compiling a focusing quality map, as was done in [33]. In the mentioned article, the quantitative criterion for the focusing quality is the width of the point spread function based on the level of half-intensity, normalized to a theoretically achievable value, so that in the presence of aberrations, the focusing quality will be less than unity. The analogous quality criterion in our article is denoted  $\delta$ . We preferred to use the RMS width of the angular intensity distribution, because it is more noise-immune.

It should be noted that if several sonograms are obtained from the same object under the same conditions, then accumulation for combating noise should be performed by averaging the angular intensity distributions of the echo signal captured at the same depth, but at different times.

## CONCLUSIONS

The article develops a new approach to detecting aberrations in ultrasound diagnostic imaging using the synthetic aperture method. In the study, a number of parameters for quantifying the presence of aberrations were investigated. From the results obtained, it can be concluded that using the proposed approach, the RMS width of the angular intensity distribution, calculated after mode subtraction, is an effective quantitative criterion for the presence of aberrations, while the use of this parameter in the conventional scheme is incorrect and prevents aberrations from being detected. A qualitative criterion for the presence of aberrations in the medium under the study is the expansion of the beam: if the beam is sufficiently narrow, there are no distortions. The paper demonstrates the possibility of detecting aberrations by the proposed method with the example of the phantom and silicone plates simulating aberrations introduced by the skull, as well as with the specimen of the temporal bone and using the data obtained during in vivo study.

The experiments were carried out at a frequency of 2 MHz and showed that the RMS width of the angular intensity distribution after mode subtraction with the appearance of aberrations increases by 22–45% with respect to the theoretical value for the case without aberrations when studies were carried out according to the proposed scanning scheme.

There are several aspects of the proposed approach that make it attractive to the ultrasound imaging community, namely, it operates with only one phased sensor and other modalities such as CT or MRI are not needed, the area under the study should not necessarily contain point sources, and it can detect aberrations in more than one area of a sonogram.

## FUNDING

This article was prepared by the team of authors as part of research (no. EGISU: AAAA-A20-120071090054-9) in accordance with the Program of the Moscow City Health Department “Scientific Support of Metropolitan Healthcare” for 2020–2022.

## ACKNOWLEDGMENTS

The authors express their deep gratitude to Prof. Lev Osipov and Sergey Skosyrev for the valuable advice and help in obtaining the raw radio-frequency signals from the pre-processing path of the ultrasound device, as well as George Grigorev, Ph.D., MD, sonologist, for examining the volunteer.

## REFERENCES

1. F. J. Fry and J. E. Barger, *J. Acoust. Soc. Am.* **63** (5), 1576 (1978).  
<https://doi.org/10.1121/1.381852>
2. G. T. Clement and K. Hynynen, *Ultrasound Med. Biol.* **28** (5), 617 (2002).  
[https://doi.org/10.1016/s0301-5629\(02\)00503-3](https://doi.org/10.1016/s0301-5629(02)00503-3)
3. O. H. Del Brutto, R. M. Mera, Andrade M. de la Luz, V. Espinosa, P. R. Castillo, M. Zambrano, and J. A. Nader, *J. Clin. Ultrasound* **44** (1), 55 (2016).  
<https://doi.org/10.1002/jcu.22284>
4. A. Y. Ammi, T. D. Mast, I. H. Huang, T. A. Abruzzo, C. C. Coussios, G. J. Shaw, and C. K. Holland, *Ultrasound Med. Biol.* **34** (10), 1578 (2008).  
<https://doi.org/10.1016/j.ultrasmedbio.2008.02.012>
5. P. B. Rosnitskiy, O. A. Sapozhnikov, L. R. Gavrillov, and V. A. Khokhlova, *Acoust. Phys.* **66** (4), 332 (2020).  
<https://doi.org/10.31857/S0320791920040097>
6. P. A. Pestova, M. M. Karzova, P. V. Yuldashev, W. Kreider, and V. A. Khokhlova, *Acoust. Phys.* **67** (3), 250 (2021).  
<https://doi.org/10.1134/S106377102103012X>
7. A. Kyriakou, E. Neufeld, B. Werner, M. M. Paulides, G. Szekely, and N. Kuster, *Int. J. Hyperthermia* **30**, 36 (2014).
8. R. Rau, D. Schweizer, V. Vishnevskiy, and O. Goksel, in *Proc. IEEE Int. Ultrasonics Symp.* (Glasgow, 2019),

- p. 2003.  
<https://doi.org/10.1109/ULTSYM.2019.8926297>
9. J. M. Escoffre and A. Bouakaz, *Therapeutic Ultrasound* (Springer, 2016).  
<https://doi.org/10.1007/978-3-319-22536-4>
  10. M. D. Eames, A. Hananel, J. W. Snell, N. F. Kassell, and J. F. Aubry, *J. Ther. Ultrasound* **1** (1), 24 (2014).  
<https://doi.org/10.1186/2050-5736-1-24>
  11. M. Mozaffarzadeh, C. Minonzio, N. de Jong, M. D. Verweij, S. Hemm, and V. Daeichin, *IEEE Trans. Ultrason., Ferroelectr. Freq. Control* **68** (1), 84 (2021).
  12. M. Ferri, J. M. Bravo, J. Redondo, and J. V. Sánchez-Pérez, arXiv:1805.10007
  13. L. Deng, A. Hughes, and K. Hynynen, *IEEE Trans. Biomed. Eng.* **67** (9), 2628 (2020).  
<https://doi.org/10.1109/TBME.2020.2967033>
  14. G. T. Clement and K. Hynynen, *Phys. Med. Biol.* **47** (8), 1219 (2002).
  15. M. Fink, *Phys. Today* **50** (3), 34 (1997).
  16. L. V. Osipov, N. S. Kulberg, S. V. Skosyrev, D. V. Leonov, G. K. Grigorev, A. V. Vladzimirskiy, and S. P. Morozov, *Biomed. Eng.* **54** (6), 438 (2021).  
<https://doi.org/10.1007/s10527-021-10057-3>
  17. B. D. Lindsey and S. W. Smith, *IEEE Trans. Ultrason., Ferroelectr. Freq. Control* **60**, 463 (2013).
  18. M. Pernot, G. Montaldo, M. Tanter, and M. Fink, *Appl. Phys. Lett.* **88** (3), 034102 (2006).  
<https://doi.org/10.1063/1.2162700>
  19. N. Wu, G. Shen, X. Qu, H. Wu, S. Qiao, E. Wang, Y. Chen, and H. Wang, *Phys. Med. Biol.* **65** (21) (2020).  
<https://doi.org/10.1088/1361-6560/abaa25>
  20. G. Maimbourg, J. Guilbert, T. Bancel, A. Houdouin, G. Raybaud, M. Tanter, and J. F. Aubry, *IEEE Trans. Ultrason., Ferroelectr. Freq. Control* **67** (10), 1993 (2020).  
<https://doi.org/10.1109/TUFFC.2020.2993718>
  21. P. B. Rosnitskiy, P. V. Yuldashev, O. A. Sapozhnikov, L. R. Gavrilov, and V. A. Khokhlova, *J. Acoust. Soc. Am.* **146** (3) (2019).  
<https://doi.org/10.1121/1.5126685>
  22. C. Jin, D. Moore, J. Snell, and D. G. Paeng, *BMC Biomed. Eng.* **2** (1) (2020).  
<https://doi.org/10.1186/s42490-020-00043-3>
  23. A. Winkler-Skalna and A. Nowoświat, *Appl. Math. Modell.* **93**, 426 (2021).
  24. S. Schoen and C. D. Arvanitis, *IEEE Trans. Med. Imaging* **39** (5), 1605 (2020).  
<https://doi.org/10.1109/TMI.2019.2953872>
  25. S. R. Haqshenas, P. Gelat, E. van't Wout, T. Betcke, and N. Saffari, *Ultrasonics* **110**, 106240 (2021).
  26. S. Almquist, D. L. Parker, and D. A. Christensen, *J. Ther. Ultrasound* **30** (4) (2016).  
<https://doi.org/10.1186/s40349-016-0074-7>
  27. L. Marsac and D. Chauvet, *Int. J. Hyperthermia* **33** (6), 635 (2017).  
<https://doi.org/10.1080/02656736.2017.1295322>
  28. N. McDannold and S. E. Maier, *Med. Phys.* **35**, 3748 (2008).
  29. N. S. Kul'berg and D. V. Leonov, RF Patent 2744313 (2021).
  30. Multi-Purpose Phantom Model ATS 539. CIRS. Data-Sheet #041621. <http://www.cirsinc.com/products/ultrasound/ats-urethane/multi-purpose-phantom/>.
  31. A. Sommerfeld, *Partial Differential Equations in Physics* (Acad. Press, New York, 1949).
  32. D. G. Duffy, *Green's Functions with Applications*, 2nd ed. (CRC Press, 2016).
  33. W. Lambert, L. A. Cobus, M. Couade, M. Fink, and A. Aubry, *Phys. Rev. X* **10** (2) (2020).  
<https://doi.org/10.1103/PhysRevX.10.021048>